

# Measurement of the $K^+ \rightarrow \pi^+ \nu \bar{\nu}$ branching fraction

A.V. Artamonov,<sup>1</sup> B. Bassalleck,<sup>2</sup> B. Bhuyan,<sup>3,\*</sup> E.W. Blackmore,<sup>4</sup> D.A. Bryman,<sup>5</sup> S. Chen,<sup>6,4</sup> I.-H. Chiang,<sup>3</sup>  
 I.-A. Christidi,<sup>7,†</sup> P.S. Cooper,<sup>8</sup> M.V. Diwan,<sup>3</sup> J.S. Frank,<sup>3</sup> T. Fujiwara,<sup>9</sup> J. Hu,<sup>4</sup> J. Ives,<sup>5</sup> D.E. Jaffe,<sup>3</sup>  
 S. Kabe,<sup>10</sup> S.H. Kettell,<sup>3</sup> M.M. Khabibullin,<sup>11</sup> A.N. Khotjantsev,<sup>11</sup> P. Kitching,<sup>12</sup> M. Kobayashi,<sup>10</sup>  
 T.K. Komatsubara,<sup>10</sup> A. Konaka,<sup>4</sup> A.P. Kozhevnikov,<sup>1</sup> Yu.G. Kudenko,<sup>11</sup> A. Kushnirenko,<sup>8,‡</sup> L.G. Landsberg,<sup>1,§</sup>  
 B. Lewis,<sup>2</sup> K.K. Li,<sup>3</sup> L.S. Littenberg,<sup>3</sup> J.A. Macdonald,<sup>4,§</sup> J. Mildenerberger,<sup>4</sup> O.V. Mineev,<sup>11</sup> M. Miyajima,<sup>13</sup>  
 K. Mizouchi,<sup>9</sup> V.A. Mukhin,<sup>1</sup> N. Muramatsu,<sup>14</sup> T. Nakano,<sup>14</sup> M. Nomachi,<sup>15</sup> T. Nomura,<sup>9</sup> T. Numao,<sup>4</sup>  
 V.F. Obraztsov,<sup>1</sup> K. Omata,<sup>10</sup> D.I. Patalakha,<sup>1</sup> S.V. Petrenko,<sup>1</sup> R. Poutissou,<sup>4</sup> E.J. Ramberg,<sup>8</sup> G. Redlinger,<sup>3</sup>  
 T. Sato,<sup>10</sup> T. Sekiguchi,<sup>10</sup> T. Shinkawa,<sup>16</sup> R.C. Strand,<sup>3</sup> S. Sugimoto,<sup>10</sup> Y. Tamagawa,<sup>13</sup> R. Tschirhart,<sup>8</sup>  
 T. Tsunemi,<sup>10,¶</sup> D.V. Vavilov,<sup>1</sup> B. Viren,<sup>3</sup> Zhe Wang,<sup>6,3</sup> N.V. Yershov,<sup>11</sup> Y. Yoshimura,<sup>10</sup> and T. Yoshioka<sup>10</sup>

(E949 Collaboration)

<sup>1</sup>*Institute for High Energy Physics, Protvino, Moscow Region, 142 280, Russia*

<sup>2</sup>*Department of Physics and Astronomy, University of New Mexico, Albuquerque, NM 87131*

<sup>3</sup>*Brookhaven National Laboratory, Upton, NY 11973*

<sup>4</sup>*TRIUMF, 4004 Wesbrook Mall, Vancouver, British Columbia, Canada V6T 2A3*

<sup>5</sup>*Department of Physics and Astronomy, University of British Columbia, Vancouver, British Columbia, Canada V6T 1Z1*

<sup>6</sup>*Department of Engineering Physics, Tsinghua University, Beijing 100084, China*

<sup>7</sup>*Department of Physics and Astronomy, Stony Brook University, Stony Brook, NY 11794*

<sup>8</sup>*Fermi National Accelerator Laboratory, Batavia, IL 60510*

<sup>9</sup>*Department of Physics, Kyoto University, Sakyo-ku, Kyoto 606-8502, Japan*

<sup>10</sup>*High Energy Accelerator Research Organization (KEK), Oho, Tsukuba, Ibaraki 305-0801, Japan*

<sup>11</sup>*Institute for Nuclear Research RAS, 60 October Revolution Prospect 7a, 117312 Moscow, Russia*

<sup>12</sup>*Centre for Subatomic Research, University of Alberta, Edmonton, Canada T6G 2N5*

<sup>13</sup>*Department of Applied Physics, Fukui University, 3-9-1 Bunkyo, Fukui, Fukui 910-8507, Japan*

<sup>14</sup>*Research Center for Nuclear Physics, Osaka University,*

*10-1 Mihogaoka, Ibaraki, Osaka 567-0047, Japan*

<sup>15</sup>*Laboratory of Nuclear Studies, Osaka University,*

*1-1 Machikaneyama, Toyonaka, Osaka 560-0043, Japan*

<sup>16</sup>*Department of Applied Physics, National Defense Academy, Yokosuka, Kanagawa 239-8686, Japan*

(Dated: October 28, 2008)

PACS numbers:

## I. INTRODUCTION

### A. $K^+ \rightarrow \pi^+ \nu \bar{\nu}$ in the standard model

### B. Interpretation of the decay $K^+ \rightarrow \pi^+$ nothing

### C. Previous results on $K^+ \rightarrow \pi^+ \nu \bar{\nu}$ below the $K_{\pi 2}$ peak

### D. The E949 detector

An extensive and detailed description of experiment E949 at Brookhaven National Laboratory has been provided elsewhere [1]. In this Section we provide a summary description of the detector and emphasize the features essential to the acquisition and analysis of data in the  $\pi \nu \bar{\nu}(2)$  region.

E949 used an incident 710 MeV/c  $K^+$  beam that was degraded and stopped in the scintillating fiber target as shown schematically in Figure 1. Observation of the decay  $K^+ \rightarrow \pi^+ \nu \bar{\nu}$  requires detection of the incoming  $K^+$  and outgoing  $\pi^+$  in the absence of any other co-incident activity. The charged pion was identified kine-

---

\*Now at Department of Physics, Indian Institute of Technology Guwahati, Guwahati, Assam, 781 039, India.

†Now at Physics Department, Aristotle University of Thessaloniki, Thessaloniki 54124, Greece

‡Now at Institute for High Energy Physics, Protvino, Moscow Region, 142 280, Russia.

§Deceased.

¶Now at Department of Physics, Kyoto University, Sakyo-ku, Kyoto 606-8502, Japan.

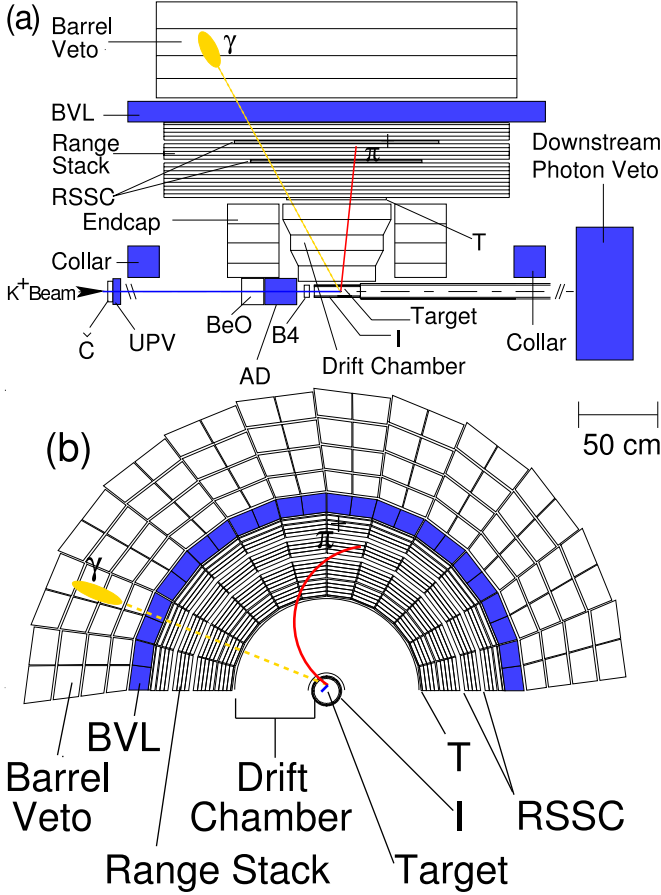


FIG. 1: Schematic side (a) and end (b) views of the upper half of the E949 detector. An incoming  $K^+$  is shown traversing the beam instrumentation, stopping in the target and decaying to  $\pi^+\pi^0$ . The outgoing charged pion and one photon from the  $\pi^0 \rightarrow \gamma\gamma$  decay are illustrated. Elements of the detector are described in the text.

matically by energy, momentum and range measurements and by observation of the  $\pi \rightarrow \mu \rightarrow e$  decay sequence. Since the  $K^+ \rightarrow \pi^+\nu\bar{\nu}$  branching fraction was expected to be at the  $10^{-10}$  level, the detector was designed to have powerful  $\pi^+$  identification to reject backgrounds from  $K^+ \rightarrow \mu^+\nu_\mu$ ,  $K^+ \rightarrow \mu^+\nu_\mu\gamma$  and  $K^+ \rightarrow \mu^+\pi^0\nu_\mu$ , photon detection coverage over  $4\pi$  solid angle to reject  $K^+ \rightarrow \pi^+\pi^0$  and  $K^+ \rightarrow \pi^+\pi^0\gamma$ , and efficient identification of a single incoming  $K^+$  to suppress beam-related background.

E949 employed a right-handed Cartesian coordinate system with  $+z$  in the incident beam direction,  $+y$  vertically upward and the polar angle  $\theta$  defined with respect to the  $+z$  axis. The entire spectrometer was immersed in a 1 T solenoidal magnetic field in the  $+z$  direction.

The incoming beam contained approximately three  $K^+$  for every  $\pi^+$  and traversed a Čerenkov counter (Č), two beam wire proportional chambers (BWPCs), a passive BeO degrader, an active degrader (AD) and a beam hodoscope (B4) as shown in Figure 1. The BWPCs are not explicitly shown in the figure. Čerenkov pho-

tons emitted by an incoming  $K^+$  ( $\pi^+$ ) passing through a lucite radiator were transmitted (internally reflected) into 14 “kaon” (“pion”) photomultiplier tubes (PMTs) to form  $C_K$  ( $C_\pi$ ) coincidences. The PMT signals are split and fed to analog-to-digital converters (ADCs), time-to-digital converters (TDCs) and amplified by ten and sent to 500 MHz charge-couple devices (CCDs) [2]. The first (second) BWPC station was located downstream of the Čerenkov counter at 168.5 (68.5) cm from the target entrance. Each BWPC station contained three planes with sense wires in the vertical and  $\pm 45^\circ$  to the vertical direction. The wire spacing in the first (second) station was 1.27 (0.80) cm. The BWPCs enabled detection of multiple beam particles. The degraders were designed such that incident kaons stopped in the center of the scintillating fiber target. The AD consisted of 40 layers of 2-mm plastic scintillator (13.9 cm diameter) interleaved with 39 2.2-mm thick copper disks (13.6 cm diameter) azimuthally divided into 12 sectors that were coupled by wavelength-shifting (WLS) fibers to PMTs that were read out by ADCs, TDCs and CCDs. These devices enabled measurement of activity in the AD coincident with the incoming beam and outgoing products of  $K^+$  decays. The B4 hodoscope downstream of the AD had two planes of 16 segmented plastic scintillator counters with 7.2-mm pitch oriented at  $\pm 33.5^\circ$  with respect to the horizontal direction. The cross-section of each counter was in a “Z” shape to minimize inactive area seen by the beam and to improve the spatial resolution. Each counter was connected to a PMT by three WLS fibers and each PMT was read out by ADCs, TDCs and CCDs. The B4 enabled a measurement of the target entry position of the beam particle as well as identification of the incident particle by energy loss.

The target was composed of 413 scintillating fibers 3.1-m long with a 5-mm square cross-section packed to form a 12-cm-diameter cylinder. A number of smaller (1-, 2-, and 3.5-mm square) “edge” fibers filled the gaps at the outer edge of the target. Each 5-mm fiber was connected to a PMT and the output PMT signals were split and input into an ADC, TDC, low-gain( $\times 1$ ) and high-gain( $\times 3$ ) CCD. Multiple edge fibers were ganged onto 16 PMTs with similar readout. Analysis of the 500 MHz sampling information provided by the target CCDs was essential for isolating and suppressing backgrounds in the  $\pi\nu\bar{\nu}(2)$  region. Two cylindrical layers of six plastic-scintillation counters defined the fiducial volume of the target. The inner layer of counters (dubbed “I counters” or “ICs”) were 6.4-mm thick with an inner radius of 6.0 cm and extended 24 cm from the upstream end of the target. The 5-mm thick outer scintillation counters (VC) overlapped the downstream end of the ICs by 6 mm and extended 196 cm further downstream. The VC served to veto particles that exited the target downstream of the IC. Each IC and VC element was instrumented with a PMT and readout by an ADC, a TDC and a 500 MHz transient digitizer(TD) [3].

The drift chamber, also called the “ultra thin chamber”

(UTC) [4], was located just outside the IC and inside the range stack as shown in Figure 1. The UTC extended radially from 7.85 cm to 43.31 cm and served to measure the trajectory and momentum of the charged track from the target to the range stack. Beginning at an inner radius of 45 cm, the range stack consisted of 19 layers of plastic scintillator counters and staggered double-layer straw chambers (RSSC) embedded after the 10<sup>th</sup> and 14<sup>th</sup> layers of scintillator. The range stack enabled the measurement of the range and energy of the charged particle, the observation of the  $\pi \rightarrow \mu \rightarrow e$  decay sequence and the measurement of photon activity. The 19 layers of plastic scintillator counters were azimuthally segmented into 24 sectors as shown in Figure 1. Layers 2-18(19) were 1.9(1.0)-cm thick and 182 cm long and were coupled on both ends to PMTs with lucite light guides. The trigger counters (T counters) in the innermost layer served to define the fiducial volume for  $K^+$  decay products and were 6.4-mm thick and 52-cm long counters coupled to PMTs on both ends by WLS fibers. The T counters were thinner than layers 2-19 to suppress rate due to photon conversions. Signals from each range stack PMT were passively split 1:2:2 for ADCs, discriminators and fan-in modules. The discriminator output was sent to TDCs and used in the trigger. The fanned-in analog sum of 4 PMTs in four adjacent sectors (dubbed a range stack “hexant”) was fed into a single TD and provided to the trigger. The TDs sample and digitize the charge in 2 ns intervals with an 8-bit resolution. The 500 MHz sampling was sufficient to resolve a  $\pi^+ \rightarrow \mu^+$  decay with a 5-ns separation between the stopping pion and the emitted muon.

Identification of  $K^+ \rightarrow \pi^+ \nu \bar{\nu}$  decays required detection of any activity coincident with the charged track. Photons from  $K_{\pi 2}$  and radiative kaon decays were detected in a hermetic photon veto system with  $4\pi$  sr solid angle coverage as shown in Figure 1. Except for the end caps, all photon veto detectors were lead-scintillator sandwich-style electromagnetic calorimeters. Essentially every scintillation counter in the experiment served as a photon veto detector. The barrel veto (BV) and barrel veto liner (BVL) covered  $2/3$  of  $4\pi$  sr in the barrel outside the range stack with a thickness 14.3 and 2.29 radiation lengths (r.l.) at normal incidence, respectively. The downstream and upstream end caps (EC) consisted of 13.5 r.l. thick undoped cesium iodide crystals and covered approximately  $1/3$  of  $4\pi$  sr [5, 6]. The upstream photon veto (UPV) was 3.1 r.l. thick and was mounted just downstream of the Čerenkov counter with an inner hole for the beam. The upstream and downstream collar counters shown in Figure 1 provided approximately 9 r.l. at normal incidence. The downstream photon veto provided 7.3 r.l. of coverage downstream of the target, EC and collar. The AD was 6.1 r.l. thick and contributed important photon veto coverage in the poorly instrumented region occupied by the incoming beam.

## II. TRIGGER

The trigger system for E949 was designed to select  $K^+ \rightarrow \pi^+ \nu \bar{\nu}$  events from the large number of  $K^+$  decays and scattered beam particles by requirements on the  $\pi^+$  range, evidence of a  $\pi^+ \rightarrow \mu^+ \nu_\mu$  decay in the range stack, lack of other detector activity at the time of the  $\pi^+$  and the presence of a  $K^+$  at an appropriately earlier time. The elements and architecture of the two-stage trigger system have been described previously [1]; we describe the features essential for the analysis of  $\pi \nu \bar{\nu}(2)$  region.

The logical OR of the following two signal triggers was used for the  $\pi \nu \bar{\nu}(2)$  analysis

$$\begin{aligned} \pi \nu \bar{\nu}(1) \equiv & KB \cdot DC \cdot (T \cdot 2 \cdot IC) \cdot (6_{ct} + 7_{ct}) \cdot \overline{19_{ct}} \\ & \cdot zfrf \cdot L0rr1 \cdot HEX \cdot \overline{(BV + BVL + EC)} \\ & \cdot L1.1 \cdot L1.2 \end{aligned} \quad (1)$$

$$\begin{aligned} \pi \nu \bar{\nu}(2) \equiv & KB \cdot DC \cdot (T \cdot 2 \cdot IC) \cdot 3_{ct} \cdot 4_{ct} \cdot 5_{ct} \cdot 6_{ct} \\ & \cdot \overline{(13_{ct} + \dots 18_{ct})} \cdot \overline{19_{ct}} \cdot L0rr2 \cdot HEX \\ & \cdot \overline{(BV + BVL + EC)} \cdot L1.1 \cdot L1.2 \end{aligned} \quad (2)$$

The  $K^+$  beam condition  $KB$  required a coincidence of at least 5  $C_K$  counters, the B4 hodoscope and at least 20 MeV of deposited energy in the target.  $T \cdot 2 \cdot IC$  required a coincidence of the first two range stack layers in the same sector with at least one IC to ensure that a charged track exited the target and entered the range stack. The delayed coincidence ( $DC$ ) required the IC time to be at least 1.5 ns later than the  $C_K$  coincidence to select kaon decays at rest. The  $\pi \nu \bar{\nu}(1)$  trigger condition  $zfrf$  required the  $z$  position of the charged track to be within the fiducial region of all traversed range stack layers. The “ $ct$ ” designation refers to the range stack  $T \cdot 2$  sector and the next two adjacent sectors that would be traversed by a positively charged particle in the magnetic field. For the  $\pi \nu \bar{\nu}(2)$  trigger, the charged track requirements  $3_{ct} \cdot 4_{ct} \cdot 5_{ct} \cdot 6_{ct} \cdot \overline{(13_{ct} + \dots 18_{ct})} \cdot \overline{19_{ct}}$  ensured hits in layers T through 6 to suppress contributions from 3-body  $K^+$  decays and vetoed on hits in the outer layers to suppress long-range charged tracks beyond the  $\pi \nu \bar{\nu}(2)$  kinematic region. The  $BV$ ,  $BVL$ ,  $EC$  and  $HEX$  requirements vetoed events with photons in the BV, BVL, EC and range stack, respectively. The  $L0rr1$  and  $L0rr2$  were refined requirements of the charged track range taking into account the number of target fibers hit and the track’s  $z$  position in layers 3, 11, 12, 13 as well as the deepest layer of penetration in order to reject long range tracks such as the  $\mu^+$  from  $K_{\mu 2}$  decay. The  $L1.1$  used the ratio of the height and area of the pulse(s) recorded by the TD to select the two-pulse signature of the  $\pi^+ \rightarrow \mu^+$  decay in the range stack counter in which the charged track was determined to have stopped. The  $L1.2$  used data digitized by the range stack ADCs to reject events with hits near the stopping counter that could falsely

satisfy the  $L1.1$  and to reject events with hits in both of the two adjacent hextants when the  $T \cdot 2$  and stopping counter were in the same sector. For the final 39% of the data taking, an online pion Čerenkov veto was included in the  $\pi\nu\bar{\nu}(2)$  trigger due to an increase in the rate of beam pions caused by a beam line malfunction.

In addition to the  $\pi\nu\bar{\nu}(2)$  and  $\pi\nu\bar{\nu}(1)$  triggers, additional “monitor” triggers were formed for calibration, monitoring, acceptance and background measurements [1]. The monitor triggers used subsets of the components of the signal trigger to predominantly select events due to  $K_{\mu 2}$  and  $K_{\pi 2}$  decays as well as scattered beam pions ( $\pi_{\text{scat}}$ ). An additional “CEX” monitor trigger requiring two  $T \cdot 2$  hits was used to collect events resulting from the charge-exchange process  $K^+n \rightarrow pK_S^0$  followed by  $K_S^0 \rightarrow \pi^+\pi^-$ . Information derived from this CEX monitor data was used as input to simulation to determine the background from charge-exchange as described in Section III C 3. In order to measure the efficiency of the  $T \cdot 2 \cdot IC$  condition, we also defined a KB monitor trigger that required  $KB$  condition described previously (Section III D).

We collectively refer to the OR of the  $\pi\nu\bar{\nu}(1)$  and  $\pi\nu\bar{\nu}(2)$  triggers as  $\pi\nu\bar{\nu}(1+2)$ .

### III. DATA ANALYSIS

#### A. Overview

Identification of the  $K^+ \rightarrow \pi^+\nu\bar{\nu}$  decay involved positive observation of the  $K^+$  and daughter  $\pi^+$  in the absence of coincident detector activity.  $K^+ \rightarrow \pi^+\nu\bar{\nu}$  has been studied in two kinematic regions dubbed “ $\pi\nu\bar{\nu}(1)$ ” and “ $\pi\nu\bar{\nu}(2)$ ” that lie above and below the  $K_{\pi 2}$  peak, respectively (Figure 2). The  $\pi\nu\bar{\nu}(1)$  and  $\pi\nu\bar{\nu}(2)$  regions in E949 extended from 211 to 229 MeV/c and 140 to 199 MeV/c in  $\pi^+$  momentum, respectively. In the  $\pi\nu\bar{\nu}(1)$  region, the background was dominated by  $K_{\pi 2}$ ,  $K_{\mu 2}$ ,  $K^+ \rightarrow \mu^+\nu_\mu\gamma$  and  $K^+ \rightarrow \pi^0\mu^+\nu_\mu$  decays and was sufficiently suppressed by positive identification of the  $\pi \rightarrow \mu \rightarrow e$  sequence and by the hermetic photon veto capability [1]. Previous studies [7, 8] in  $\pi\nu\bar{\nu}(2)$  region identified the main background as due to  $K_{\pi 2}$  decays in which the charged pion scatters in the target, loses energy and falls into the signal region above the  $K \rightarrow 3\pi$  endpoint and below the  $K_{\pi 2}$  peak. Additional lesser sources of kaon decay background with the  $\pi^+$  in the  $\pi\nu\bar{\nu}(2)$  region included  $K^+ \rightarrow \pi^+\pi^0\gamma$  ( $K_{\pi 2\gamma}$ ) and  $K^+ \rightarrow \pi^+\pi^-e + \nu_e$  ( $K_{e4}$ ). Successful analysis of the  $\pi\nu\bar{\nu}(2)$  region relied on the photon veto capability and, in contrast to the  $\pi\nu\bar{\nu}(1)$  analysis, identification of the scattering process or the presence of additional particles in the target. The  $\pi\nu\bar{\nu}(2)$  region has a larger potential acceptance than  $\pi\nu\bar{\nu}(1)$  because the phase space is larger and the loss of  $\pi^+$  due to nuclear interactions in the detector is smaller at lower pion energies. These factors

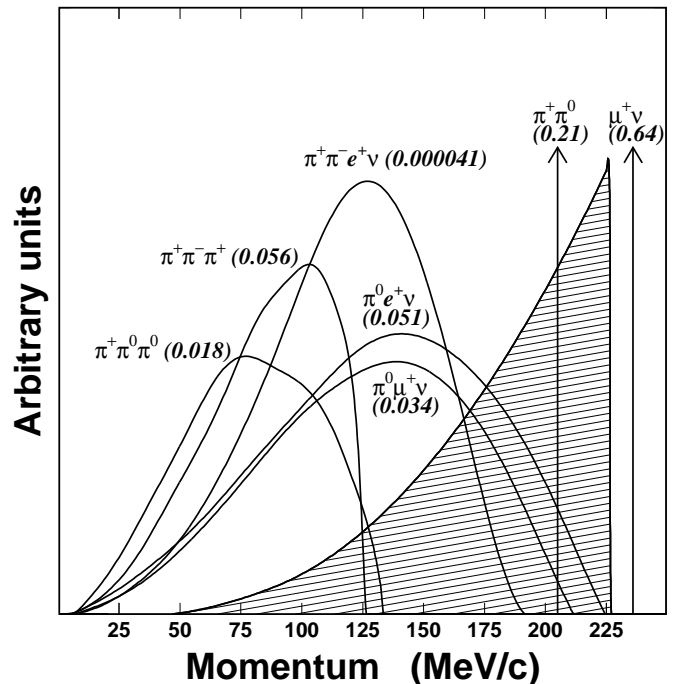


FIG. 2: Momentum spectra of charged particles from  $K^+$  decay in the rest frame. The values in parentheses represent the branching fractions of the decay modes [9]. The hatched spectrum represents the  $\pi^+$  spectrum from  $K^+ \rightarrow \pi^+\nu\bar{\nu}$  decay assuming the  $V - A$  interaction.

partially mitigate the loss of the acceptance due to these additional requirements needed to suppress background.

#### 1. Kaon decay background

The largest background contribution in the  $\pi\nu\bar{\nu}(2)$  region was due to  $K_{\pi 2}$  decay in which the charged pion experienced a nuclear interaction near the kaon decay point, probably on a carbon nucleus in the plastic scintillator of the target. The reduced kinetic energy due to the scatter put the pion in the  $\pi\nu\bar{\nu}(2)$  region. In addition, the scatter obscured the directional correlation between the charged and neutral pion, thus directing the photons from  $\pi^0$  decay away from the barrel region of the photon veto. This background was suppressed by recognition of the scattering process in the target. A smaller background contribution due to scattering of the charged pion in the range stack was suppressed by track pattern and energy deposit in the range stack. The photon veto served to suppress these “ $K_{\pi 2}$ -scatter” backgrounds as well as background due to the radiative decay  $K_{\pi 2\gamma}$ . Background due to  $K_{e4}$  was suppressed by identification of additional particles in the target. Kaon decays with a muon in the final state,  $K_{\mu 2}$ ,  $K^+ \rightarrow \mu^+\nu_\mu\gamma$  and  $K^+ \rightarrow \pi^0\mu^+\nu_\mu$ , were suppressed by kinematics and the recognition of the  $\pi \rightarrow \mu \rightarrow e$  signature as well as the photon veto for the latter two decays.

## 2. Beam-related background

The beam-related backgrounds were categorized into single- and double-beam background and CEX background. The CEX background occurred due to the production of a  $K^0$  in the target due to the charge-exchange process  $K^+n \rightarrow pK^0$ . If the  $K^0$  turned into a  $K_L^0$  that subsequently underwent semileptonic decay, the  $\pi^+$  could fall in the  $\pi\nu\bar{\nu}(2)$  kinematic region. CEX background was rejected by observing the gap between the  $K^+$  and  $\pi^+$  fibers due to propagation of the non-ionizing  $K_L^0$ , by the inconsistency between the energy deposited by the  $K^+$  and the reconstructed  $z$  of the outgoing pion and by identification of the accompanying negative lepton. In addition, requirements on the delayed coincidence between the  $K^+$  and  $\pi^+$  suppressed CEX background due to the short  $K_L^0$  flight time.

Single-beam background could have been due to a  $K^+$  entering the target and decaying in flight to produce a  $\pi^+$  in the  $\pi\nu\bar{\nu}(2)$  region. Incoming beam  $\pi^+$ , misidentified as  $K^+$ , and scattering in the target also contributed to the single-beam background. Positive identification of the incoming particle as a kaon as well as requirements on the delayed coincidence between the incoming and outgoing tracks suppressed the single-beam background.

The two processes that contributed to single-beam background, kaon decay-in-flight and pion scattering, formed the double-beam background when preceded by an additional incoming kaon whose decay products were undetected. Double-beam background was suppressed by requiring a lack of activity in the beam and target in coincidence with the  $\pi^+$  detected in the range stack.

## 3. Analysis method and strategy

We used analysis procedures and strategies similar to that of the E949 analysis of the  $\pi\nu\bar{\nu}(1)$  region [1] with some extensions that took into account the difficulty of isolating some background samples in the data in the  $\pi\nu\bar{\nu}(2)$  region. As with the previous analysis, we adopted a “blind” analysis method in that we did not examine the pre-defined signal region until all background and acceptance analysis was completed. Since we also attempted to perform all background estimates directly from the data, we inverted at least one selection criteria (“cut”) when we used the  $\pi\nu\bar{\nu}(1+2)$  data to avoid examining the signal region. Every third  $\pi\nu\bar{\nu}(1+2)$  trigger formed the “1/3” sample that was used to determine the selection criteria. We then obtained unbiased background estimates by applying the finalized selection criteria to the remaining “2/3” sample of  $\pi\nu\bar{\nu}(1+2)$  triggers.

The preferred method of background estimation employed the bifurcation method illustrated in Figure 3. The parameter space of two cuts “CUT1” and “CUT2” can be divided into the four regions shown in the figure by the application of each cut or the inverted cut. For example, the number of events in the signal region

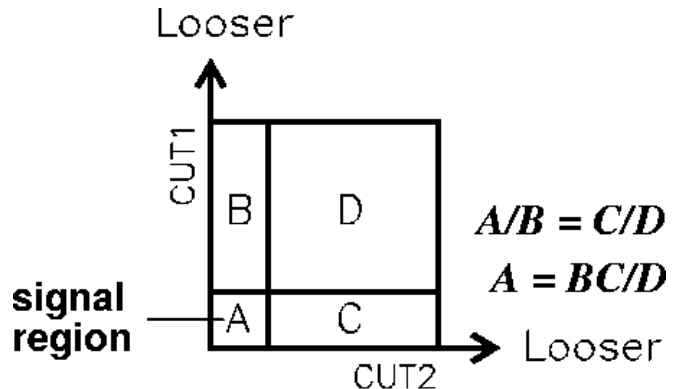


FIG. 3: Schematic of the bifurcation method. The background level in region A can be estimated from the number of events observed in the other regions assuming CUT1 and CUT2 are uncorrelated.

“A” can be determined by application of both CUT1 and CUT2. If the rejection of CUT1 does not depend on CUT2 and vice versa, then the number of events in A can be estimated as the number of events in region B times the ratio of the number of events in regions C and D or  $A = BC/D$ . In practice, we employed two branches for the bifurcation analysis. The “normalization branch” analysis was performed to obtain the number of events,  $N_{\text{norm}}$ , in region B. A “rejection branch” analysis was used to obtain  $D/C$ . We defined the rejection as  $R \equiv (C + D)/C$  and obtained the background estimate as  $N_{\text{bkg}} = N_{\text{norm}}/(R - 1)$ . For all background estimates in this analysis, the normalization branch was taken from the  $\pi\nu\bar{\nu}(1+2)$  data. We used the  $\pi\nu\bar{\nu}(1+2)$  data to obtain the rejection branch for all backgrounds except for the CEX,  $K_{e4}$  and  $K_{\pi 2\gamma}$  backgrounds that could not be cleanly isolated in data. When no events ( $N_{\text{norm}} = 0$ ) were available in the normalization branch, we conservatively assigned  $N_{\text{norm}} = 1$ .

We checked the validity of the background estimates by loosening cuts and comparing the predicted the number of events just outside the signal region with observations (Section III C 7). In addition we examined events passing a single major selection criteria to search for unforeseen background sources and coding mistakes (Section III C 8).

## B. Data selection requirements

Event reconstruction was performed in a number of steps consisting of track-fitting in various detector systems such as the beam-line detectors, the range-stack, the UTC and the target. Multiple iterations of the track-fitting were performed in many of the detector systems using progressively better information from track-fitting from other detector systems as constraints. The following discussion focuses on the target track-fitting to clearly define the target-fiber classification scheme for use in the

description of the target CCD fitter and descriptions of the cuts using target fiber information.

After UTC track-fitting was performed, target fibers were clustered into  $K^+$  and  $\pi^+$  paths based on geometry, energy and timing information. The  $\pi^+$  fibers had to lie along a strip (typically 1 cm in width) along the UTC track extrapolated into the target, have an energy between 0.1 and 10.0 MeV and be in coincidence with  $t_{rs}$ . The  $K^+$  fibers had to have greater than 4 MeV of energy and be coincident with the beam strobe (FIXME - is beam strobe defined?). Any fiber that did not fall into the  $K^+$  or  $\pi^+$  fiber categories, but that fell within  $\pm 5ns$  of  $t_{rs}$  (FIXME - double-check this timing window with Benji), were classified as  $\gamma$  fibers if they had more than 0.1 MeV of energy. The designation of each fiber as a  $\pi^+$  and  $\gamma$  fiber could be switched based on likelihood values calculated from energy, time and distance from the extrapolated UTC track. The event failed target reconstruction if there was more than one  $K^+$  or  $\pi^+$  path, or if these two paths were not geometrically adjacent in the  $x-y$  plane. The decay vertex was identified in the  $K^+$  fiber closest to the extrapolated UTC track and furthest away from the  $x-y$  position of the B4 hit. The average times of the  $K^+$  and  $\pi^+$  hits were defined as  $t_K$  and  $t_\pi$ , respectively. The sums of the  $K^+$  and  $\pi^+$  energies were defined as  $E_K$  and  $E_\pi$ , respectively. FIXME - Still need to add something about opposite-side pion fibers. FIXME - Add something about B4 information not being used in early iterations, but being used in later iterations?

Using the target CCD fitter, the activity in each of the target fibers was fit using a single-pulse and double-pulse assumption. If there was second-pulse energy coincident with  $t_\pi$  in the vertex fiber, this energy was subtracted from  $E_K$  and added to  $E_\pi$ .

For each channel of each fiber (FIXME - low-gain and high-gain target CCD channels need to be defined), a standardized  $K^+$  pulse used for the target CCD fitter was created using  $K^+$  fiber data from  $K_{\mu 2}$  monitor trigger data. For each fiber having an energy greater than a fiber-dependent threshold, the fitting procedure was performed on the low-gain and the high-gain CCD information independently. A single-pulse fit was attempted for each fiber channel passing the above criteria. The single-pulse fit used two parameters, the  $K^+$ -pulse amplitude and the time. Pedestal subtraction had already occurred previous to the target CCD fitter so the pedestal was not included in the fit. If the probability of the single-pulse fit was less than 25%, a double-pulse fit was performed. The double-pulse fit used a second copy of the standardized  $K^+$  pulse for that fiber and added it to the first pulse, where the amplitude and time offset could be varied relative to the first pulse. The double-pulse fit used four parameters, the amplitudes and times for each of the  $K^+$  and  $\pi^+$  pulses. These least-squares fits were performed by varying the above-mentioned parameters.

### 1. Requirements on $\pi^+$ in the target

#### Target pulse data analysis

*Pion energy from target CCD fitting:* The second-pulse activity in a  $K^+$  fiber as found by the target CCD fitting was required below 1.25 MeV when it was coincident with  $\pi^+$  activity in the target. This cut had three sequential stages. In the first stage, the low-gain and high-gain CCDs of each  $K^+$  fiber were examined to determine if a double-pulse fit had been successfully performed. In the second stage, an algorithm determined if the information from the high-gain CCD, the low-gain CCD or a combination of the two should be used for each fiber that had successful double-pulse fits. In the third stage, each fiber from the second stage was examined for second-pulse energies above 1.25 MeV and rejected the event if the second pulse ( $t_2$ ) was coincident with  $\pi^+$  activity in the target ( $t_\pi$ ), where the coincidence condition was  $-7.5 \text{ ns} \leq t_2 - t_\pi \leq 10 \text{ ns}$ .

*Bad fit results from target CCD fitting:* It was required that the target CCD fitter successfully fit each of the  $K^+$  fibers having an energy larger than 1.25 MeV. A fit was considered successful if the probability was above zero for the fits performed with either the single-pulse or the double-pulse assumption. (FIXME - talk about the three stages as was done for CCDPUL?)

*Bad timing results from target CCD fitting:* It was required that the time of the  $K^+$  pulse found by the target CCD fitter was consistent with  $t_K$  for  $K^+$  fibers having more than 1.25 MeV of energy. This cut was designed as a safety cut to remove events where the target CCD fitter found a known incorrect solution with a probability greater than zero. These known incorrect solutions occurred when the fitter attempted to fit a fluctuation in the tail of the reference pulse to the pulse being fit or when there was a large second pulse in the fiber being fit and the fitter mistakenly identified it as the first pulse. If only the single-pulse fit was performed (the single-pulse fit solution had a probability greater than 0.25), the single-pulse time was required to be coincident with  $t_K$  ( $-6 \text{ ns} < t - t_K < 7 \text{ ns}$ ) and to be greater than  $-9.98 \text{ ns}$ . If both the single-pulse and double-pulse fit were performed, the  $K^+$  pulse from the double-pulse fit was required to be coincident with  $t_K$  ( $-6 \text{ ns} < t - t_K < 7 \text{ ns}$ ) and to be greater than  $-9.98 \text{ ns}$ , and the  $\pi^+$  from the double-pulse fit was required to be greater than  $-4.99 \text{ ns}$ . These minimum times were associated with the earliest physical times stored in the ntuple (FIXME - jargon alert!) by the target CCD fitter.

*Maximum fibers used for target CCD fitting:* The 31st fiber fit by the target CCD fitter was required to have a fit probability for the single-pulse assumption of greater than 0.25. This was a safety cut created to deal with a storage error associated with the target CCD fitter that occurred only for events where more 31 or more fibers were fit.

## PNN2 tgcuts placeholder (FIXME)

*Time, energy and position cut for  $K^+$  fibers:* The target  $K^+$  fiber hits were required to be consistent with a kaon approaching the  $K^+$  decay vertex. This consistency was checked by tabulating the times of the kaon fiber hits against the distance to the decay vertex in the  $x$ - $y$  plane and against the range of the kaon as determined by deposited energy.

*Extreme target pion energies:* The total energy of the  $\pi^+$  target fibers was required to be in the range of 1 to 28 MeV.

*Tag gaps between  $K^+$  and  $\pi^+$  tracks:* This cut was not used to define the signal region, but was instead used to identify pion tracks which did not emerge directly from the target  $K^+$  fibers. This cut, used in the charge exchange background evaluation (see Section xxx FIXME), was designed to provide a cleaner sample of this type of event than that produced by inverting TARGF (FIXME - won't be called TARGF). The target reconstruction algorithm identified potential  $\pi^+$  target fibers having large energy deposits as photon fibers. Allowing these photon fibers within 3.0 ns of  $t_{rs}$  to fill the gap created a cleaner sample of events having true gaps between the  $K^+$  and  $\pi^+$  fibers.

*Quality of target  $\pi^+$  track:* The target  $\pi^+$  track fitter and target  $\pi^+$  fibers were required to be consistent as enforced by a probability determined from the sum of three  $\chi^2$ -like quantities. These  $\chi^2$ -like quantities had contributions from target pion fibers and the target  $\pi^+$  track fitter as follows:

1. Contributions for hit  $\pi^+$  fibers which were part of the reconstructed target  $\pi^+$  track were based on observed versus expected energy.
2. Contributions for target fibers with no energy, but lying along the projected target  $\pi^+$  track were based on the minimum distance between the projected track and the corners of the fiber. This forced the fitted track to go between the fibers.
3. Contributions for hit target  $\pi^+$  fibers which were not part of the reconstructed target  $\pi^+$  track were based on their distance from the track.

*Maximum contribution to the target fitter  $\chi^2$ :* The first  $\chi^2$ -like quantity from the quality of target  $\pi^+$  track cut was required to be below a certain threshold.

*Pion energy under target fiber classified as both a  $K^+$  and  $\pi^+$  fiber:* Target fibers classified as both a  $K^+$  and a  $\pi^+$  target fiber were required to have less than 1.25 MeV assigned to the pion pulse. The target reconstruction was able to find pion hits in  $K^+$  fibers when the  $\pi^+$  activity occurred at least 15 ns later than the  $K^+$  activity.

*Matching target track fit with vertex fiber:* The  $\pi^+$  track from the target reconstruction was required to intersect the  $K^+$  vertex fiber, also identified by target reconstruction.

## PNN1 tgcuts placeholder (FIXME)

*Target energy loss:* The deposited energies per unit length in the target were required to be consistent with that of a  $\pi^+$ . This cut used a likelihood function based on the following quantities of the  $\pi^+$  track: momentum ( $ptot$ ), range in the target,  $\pi^+$  energy deposited in the target and expected range in the target based on the measured energy deposited in the target and the momentum  $ptot$ . This suppressed backgrounds where the charged track was due to a lepton, such as muon-based backgrounds.

*Target gap between  $K^+$  and  $\pi^+$  fibers:* The minimum distance between the target  $K^+$  and  $\pi^+$  was required to be less than the width of a single target fiber (0.6 cm). This cut suppressed CEX and double-beam backgrounds.

*Consistency between UTC and target track fitting:* The angle between the track from target reconstruction and from the UTC extrapolated track was required to be less than 0.01 radian when the range of the  $\pi^+$  in the target was less than 2.0 cm. and the UTC extrapolated track was greater than 0.01 radian.

*Target  $\pi^+$  fiber energy:* Target fibers classified as  $\pi^+$  fibers were required to have energies less than 3.0 MeV. This suppressed  $\pi^+$  target-scatters since the nominal energy deposited in a  $\pi^+$  fiber was 1.2 MeV.

*Target back-to-back tracks:* Event was rejected if it had back-to-back charged decay-product tracks in the target.

*Opposite-side  $\pi^+$  fibers:* The total energy in the target opposite-side  $\pi^+$  fibers within  $\pm 4.0$  ns of  $t_\pi$  was required to be less than 1.0 MeV. If the likelihood from the beam likelihood cut was below a certain threshold, the total energy was required to be less than 0.5 MeV.

*Matching between target and UTC tracks:* The reconstructed  $\pi^+$  tracks in the target and UTC were required to be well-matched at the target edge.

*Quality of target path length calculation:* The uncertainty in the calculation of the target  $\pi^+$  path length was required to be less than 1.5 cm.

*Target kink from UTC extrapolation:* Kinks in the target  $\pi^+$  track were suppressed by requiring that there was a small spread between the minimum and maximum radius of the UTC reconstructed track.

*Energy in target edge fibers:* The total energy within  $\pm 5.0$  ns of  $t_{rs}$  in a set of multiplexed target edge-fibers was required to be less than 4.0 MeV.

*Decay vertex and  $K^+$  cluster position consistency with B4 and  $\pi^+$  fibers:* Three requirement conditions were used to enforce consistency between the positions of the target kaon decay vertex, the kaon and pion clusters, and the beam particle in the B4 Hodoscope. The first condition required that the distance in the  $xy$ -plane between the hit position in the B4 Hodoscope and the nearest tip of the target  $K^+$  cluster. The  $K^+$  cluster tips were the two  $K^+$  fibers furthest apart from each other. The second condition required that the distance in the  $xy$ -plane between the  $K^+$  decay vertex identified from target reconstruction and the nearest  $K^+$  cluster tip was less than

0.7 cm. The third condition required that the distance in the  $xy$ -plane between the  $K^+$  decay vertex and the nearest  $\pi^+$  fiber was less than 1.5 cm.

## 2. Pion track requirements

Three quantities were reconstructed with pion assumption, more information could be found in [1]. They were total momentum  $P_{tot}$ , total energy  $E_{tot}$  and total range  $R_{tot}$  in plastic scintillator.  $R_{tot}$  was determined as follows:

$$R_{tot} = R_{TG} + R_{IC} + R_{UTC} + R_{RS}$$

where  $R_{TG}$  was the measured  $\pi^+$  range in the target,  $R_{IC}$  the range in I-counter,  $R_{UTC}$  the range in the UTC inner and outer carbon fiber walls and  $R_{RS}$  was the range in the range stack.

The UTC track was reconstructed by two separate fits: one in the  $xy$  plane and the one in the  $rz$  plane. In the  $xy$  plane a circle was fitted to the hit positions derived from the wire locations and drift distances. In the  $rz$  plane a straight line was fitted to the cathode strip hits. The polar angle of the charged track was evaluated from this  $rz$  fitting. The  $K_{\pi 2}$  target scattering background was the largest background in  $\pi\nu\bar{\nu}(2)$  analysis. Some pion fiber and vertex fiber might not be aligned with pion track due to scattering. To avoid the momentum to be messed by the scattering, information from fired fibers were not used in the UTC fit. The measured drift chamber was then corrected for the energy loss by the  $\pi^+$  before leaving the target, I-counter and the inner wall of UTC.

The total  $\pi^+$  energy was given by

$$E_{tot} = E_{TG} + E_{IC} + E_{UTC} + E_{RS}$$

where  $E_{TG}$  was the measured  $\pi^+$  energy in the target,  $E_{IC}$  the energy measured in the I-counter,  $E_{UTC}$  the energy deposited in the drift chamber walls and  $E_{RS}$  the energy measured in the range stack.

**UTC track quality:** Good track reconstruction was required based on the  $\chi^2$  of UTC track fit. When there were tracks overlapping in the UTC or when there were less fired hits available for the fit the momentum resolution was getting worse. More stringent requirement was enforced on the  $\chi^2$ .

**Matching between range stack track and UTC track extrapolation:** Reject the events if the matching of UTC track extrapolation with the fired counters' energy and position in range stack or RSSC was poor.

**Beam likelihood:** (**BAD NAME**) The  $K^+$  track with certain momentum would leave certain energy in B4 Hodoscope. The energy deposit in the B4 should be consistent with the energy sum of the kaon fibers and the  $K^+$  stopping  $z$  position. The  $z$  position was determined by UTC track extrapolation.

**Target fiducial requirement:** Event was rejected if the  $z$  position of the kaon decay vertex was too close the

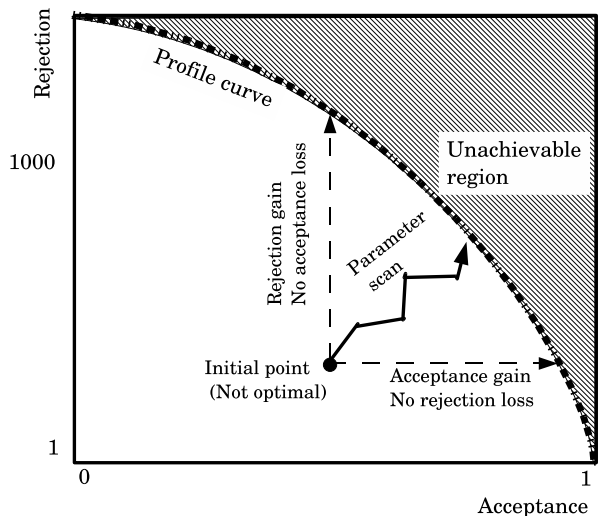


FIG. 4: Illustration of the optimization process to determine the photon veto parameters.

upstream end of the target or was not in the fiducial region of the target at all. This  $z$  position was determined by UTC track extrapolation.

## 3. Photon veto requirements

Photon veto requirements were fulfilled within a subsystem when the sum of activity occurring within a time window exceeded an energy threshold. The time window and energy threshold was set in BV, BVL, RS, EC, EC<sub>inner</sub> (the inner ring of the upstream EC was considered a separate category due to having higher accidental rates than the remaining EC elements.), EC<sub>2nd</sub> (**FIXME: reasons**), target, IC, VC, CO,  $\mu$ CO by an optimization algorithm as diagramed in Figure 4 and further described in [1].

The  $\pi\nu\bar{\nu}(1)$  set of parameters, as listed in Table VI of [1], was the starting point for the  $\pi\nu\bar{\nu}(2)$  PV parameter optimization. The optimization process measured the rejection and acceptance as the time window and energy threshold were varied. The optimization goal was to maximize rejection or acceptance without causing a decrease in the acceptance or rejection, respectively, until no further gain was possible. The profile of the maximum rejection for a given acceptance for the  $\pi\nu\bar{\nu}(2)$  optimization is shown in Figure 5.  $K_{\pi 2}$  target-scatter events would have been the ideal rejection sample, but due to a lack of statistics  $K_{\pi 2}$  events were chosen as the rejection sample, while the acceptance sample was from  $K\mu 2$  monitor events as chosen in the optimization of  $\pi\nu\bar{\nu}(1)$  analysis. Validation of the PV requirements that were optimized were performed on various classes of  $K_{\pi 2}$  target-scatter and kinks **FIXME: how are we saying kinks, defined previously?**.

The BV was unable to determine the correct time of



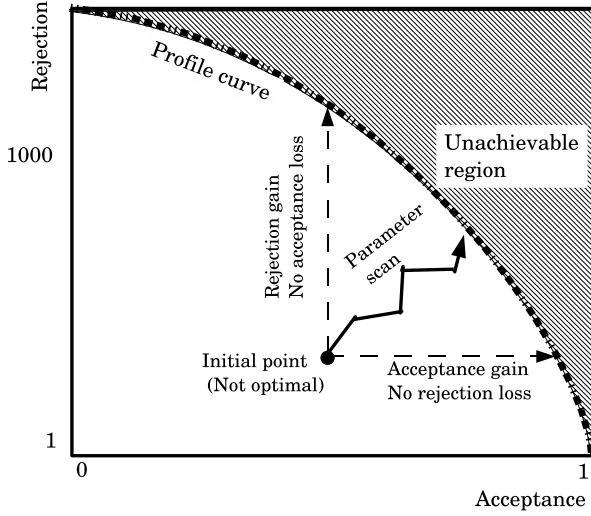


FIG. 5: Offline rejection of photon veto cuts as a function of the acceptance. The vertical lines show the position of the two cut positions used for the nominal and tight regions in pnn2 analysis. **FIXME: obtain correct figure**

photon activity when proceeded by an accidental hit not associated with the kaon decay. The criteria ( $BV_{early}$ ) was created to reject events when any individual BV counter had activity greater than 30 MeV within the time window shown in row 12 of Table I. The  $BV_{early}$  parameters were chosen using the previous mentioned rejection and acceptance samples after the application of the all PV categories listed in rows 1-11 of Table I.

TABLE I: Time window and energy threshold for category of the photon veto cuts.

Category	Nominal		Tight	
	Time window (ns)	Energy (MeV)	Time window (ns)	Energy (MeV)
BV	[-5.70,10.20]	0.20	[-7.50,10.20]	0.70
BVL	[-4.40,10.70]	0.30	[-3.50,10.60]	0.30
RS	[-4.25,4.35]	0.30	[-3.30,7.80]	0.60
EC	[-4.35,7.95]	0.40	[-6.00,9.50]	0.20
EC <sub>inner</sub>	[-3.65,5.63]	0.20	[-14.00,9.10]	0.20
EC <sub>2nd</sub>	[-5.67,2.47]	10.60	[-5.70,2.68]	0.20
TG	[-2.65,2.15]	2.00	[-6.55,2.25]	1.70
IC	[-2.00,4.50]	5.00	[-2.90,9.30]	1.40
VC	[-6.55,1.75]	6.80	[-7.45,7.05]	5.00
CO	[-0.05,5.85]	0.60	[-0.80,5.10]	6.00
$\mu$ CO	[-5.50,2.30]	3.00	[-4.50,3.30]	1.60
$BV_{early}$	[-35.70,-5.70]	30.00	[-37.50,-7.50]	30.0
AD	[-2.00,8.00]	0.60	[-2.00,8.00]	0.60
DSPV	[-5.00,10.00]	0.00	[-5.00,10.00]	0.00
$BV_{early}$	[-5.00,-2.00]	10.00	[-5.00,-2.00]	10.00

Photon veto parameters for the AD and DSPV were not able to be optimized with the same rejection sample as previously mentioned due to these systems only

being sensitive to photons with small  $\theta$  **FIXME:  $\theta$  defined?**. For the AD parameters a rejection sample composed of kinks (SKIM8 **FIXME: where to define SKIM8/kink sample?**) with the cuts associated with the optimized PV parameters in row 1-12 of Table I at 90% acceptance (not listed in Table). The rejection sample to optimize DSPV's parameters also utilized kink events.

When both photons from a  $\pi^0$  converted in the same BVL counter the reconstructed time was earlier than the true time and the  $z$  position was near the center of the counter ( $z \simeq 0$ ), as determined by averaging the times of hits on each end, rather than near the edge of the counter. Due to geometric constraints, this was only possible when the photons converted at opposite ends of the BVL counter. To remove this possible scenario from being a background, events with a BVL hit with times within the range  $[-5.0,-2.0]$  ns, a reconstructed  $z$  value of less than 4.0 cm, and energy greater than 10.0 MeV were removed. Although this cut ( $BV_{early}$ ) was observed to have no acceptance loss after all cuts and no rejection after all other PV cuts were applied,  $BV_{early}$  was employed as a “safety” cut.

The collection of cuts associated with the categories in Table I was referred to as PV cuts. As seen in Figure 5, a loose and tight version of PV cuts were chosen at acceptances of 60% and 30%, respectively. Parameters of some subsystems became looser at lower values of acceptance because the optimization process did not constrain the time window or energy threshold based upon previously chosen parameters and mutual correlations among subsystems. To guarantee that the tight PV cut was tighter for all subsystems than the nominal PV cut, the tight PV cuts were defined to be the application of PV cuts associated with both sets of parameters.

shows the rejection as a function of acceptance for pnn2 optimization. Two sets of parameters were

#### 4. Decay pion kinematic requirements

(explain  $ptot$ ,  $etot$ ,  $rtot$ ? **FIXME**) Better energy and range resolutions in Range Stack were achieved by employing  $X_e$  monitoring system to calibrate Range Stack. Because the largest background was from  $K_{\pi 2}$  target scattering while not  $K_{\pi 2}$  events directly the strategy of setting kinematic search region in  $\pi\nu\bar{\nu}(1)$  analysis was used. The upper limits of kinematic search region were chosen to be  $ptot \leq P_{K_{\pi 2}} - 2.5\sigma_P$  (199 MeV/c),  $etot \leq E_{K_{\pi 2}} - 2.5\sigma_E$  (100.5 MeV) and  $rtot \leq R_{K_{\pi 2}} - 2.75\sigma_R$  (28cm) where  $P_{K_{\pi 2}}$ ,  $E_{K_{\pi 2}}$  and  $R_{K_{\pi 2}}$  were the  $K_{\pi 2}$  kinematic peak and  $\sigma_P$ ,  $\sigma_E$  and  $\sigma_R$  were the corresponding resolutions. To suppress background from  $K^+ \rightarrow \pi^+\pi^+\pi^-$  and  $K^+ \rightarrow \pi^+\pi^0\pi^0$  and implicitly determined by the minimum range requirement of the  $K \rightarrow \pi\nu\bar{\nu}$  trigger the lower limits were set to  $ptot > 140\text{MeV}/c$ ,  $etot > 60\text{MeV}$  and  $rtot > 12\text{cm}$ . Larger acceptance was achieved in this analysis partly by a bigger

search region.

A tighter kinematic search region was defined within the normal search region to further suppress  $K_{\pi 2}$  and  $K_{e4}$  background which were the first and second largest background. The momentum distribution of  $K_{\pi 2}$  and  $K_{e4}$  events were not uniformly distributed in the signal region. The  $K_{\pi 2}$  target scattering events formed a tail at the lower end of  $K_{\pi 2}$  momentum peak and it was obvious that most events had very little momentum changed.  $K_{e4}$  background momentum tended to gather around 160 MeV/c as explained in section III C 2 and Fig. 7 where the kinematic and trigger acceptance of  $K \rightarrow \pi \nu \bar{\nu}$  was decreasing. Through optimization performed on acceptance versus the sum of the  $K_{\pi 2}$  and  $K_{e4}$  background the tighter kinematic region was set to  $165 \leq p_{tot} \leq 197(\text{MeV}/c)$ ,  $72 \leq e_{tot} \leq 100(\text{MeV})$  and  $17 \leq r_{tot} \leq 28(\text{cm})$ .

### 5. Delayed coincidence requirements

Determining that the incoming  $K^+$  stopped within the target was accomplished by observing a delay in the outgoing charged track which was presumed to be a  $K^+$  decay product. This requirement would remove beam  $\pi^+$  scattering events and  $K^+$  decay-in-flight events. The delayed coincidence requirements were split into a loose version and a tight version.

In the loose version the average time of the kaon fiber hits ( $t_K$ ) and the average time of the pion fiber hits ( $t_\pi$ ) was required to meet the minimum delayed coincidence requirement of 3 ns. Additional constraints were placed on it when the timing consistency between detector systems was degraded. It was tightened to 4 ns when the energy deposit in the target kaon fibers was less than or equal to 50 MeV or when the time of any of the individual kaon fiber differed from the average time the kaon fiber hits by more than 2 ns or when the time of any of the individual target pion fibers differed from the average time of the pion fiber hits by more than 3.5 ns. It was tightened to 5 ns when the difference between the  $t_K$  and the B4 Hodoscope hit time was greater than 1 ns or when  $t_\pi$  was determined using I-Counter hit time instead of the average time of the pion fiber hits. It was tightened to 6 ns when the difference between  $t_\pi$  and track time in the Range Stack was greater than 1.5 ns. In the tight version 6 ns delayed coincidence requirement was employed for the use in a signal region with reduced background.

## C. Evaluation of backgrounds

### 1. $K_{\pi 2(\gamma)}$ background

The total  $K_{\pi 2(\gamma)}$  background was determined from estimates of three separate background modes:  $K_{\pi 2}$  target-scatter,  $K_{\pi 2}$  range-stack-scatter and  $K_{\pi 2(\gamma)}$ . For a  $K_{\pi 2}$  event to have appeared in the signal region, the photons from the  $\pi^0$  decay had to escape detection and the  $\pi^+$

had to lose some undetected energy via scattering or resolution effects such that it fell into the signal phase space. This scattering could happen in the target ( $K_{\pi 2}$  target-scatter) or in the range stack ( $K_{\pi 2}$  range-stack-scatter), but the target-scatter component dominated. Since the  $\pi^+$  from a  $K_{\pi 2(\gamma)}$  decay is not monochromatic, only the three photons needed to escape detection for this type of event to have appeared in the signal region.

The topology of the most problematic type of  $K_{\pi 2}$  target-scatter was that of a  $\pi^+$  initially traveling along the same target fibers in which the kaon deposited energy and scattering into the active region of the detector. The first reason that this type of target-scatter was difficult to reject was that some energy deposited in the target by the scattering  $\pi^+$  was hidden in a kaon (FIXME define kaon fiber or explain another way?) fiber. The second reason that this type of target-scatter was difficult to reject was a consequence of the  $\pi^+$  and  $\pi^0$  emerging back-to-back. A  $\pi^+$  initially traveling along the kaon fibers meant that the  $\pi^0$  was also traveling parallel to the beam direction and the resulting photons from its decay were directed at the upstream or downstream ends of the detector where the photon veto is weakest.

In the  $K_{\pi 2}$  target-scatter background study, the two bifurcation cuts were chosen as the PV cuts (CUT1) and the target-quality cuts (CUT2) since both of these could give powerful rejection of the  $K_{\pi 2}$  target-scatter background. In order to remove the contamination from muon and beam events (FIXME and charge exchange?), the bifurcation analysis sample was selected by applying the TD, beam and KIN cuts. In the normalization branch, a combination of  $K_{\pi 2}$  target-scatter,  $K_{\pi 2}$  range-stack-scatter and  $K_{\pi 2(\gamma)}$  events were selected by inverting the PV cut ( $\overline{\text{CUT1}}$ ). All target quality cuts (CUT2) were applied to the sample, resulting in 1131 events left in the normalization branch. After corrections for  $K_{\pi 2}$  range-stack-scatter contamination,  $B = 1107.7 \pm 33.8^{+2.9}_{-2.8}$  events remained in the normalization branch, where the first error is statistical and the second error is systematic (FIXME explain where the systematic error comes from). Corrections for contamination due to  $K_{\pi 2(\gamma)}$  contamination are discussed later in this section. In the rejection branch,  $K_{\pi 2}$  target-scatter events were selected by (FIXME long giant thing about the classes making appropriate rejection samples and somewhat in-depth discussion of the classes), giving 52 621 events for the region C + D. The PV cuts (CUT1) were then applied to the remaining  $K_{\pi 2}$  target-scatter events, leaving 22 events for the region C.

For the  $K_{\pi 2}$  range-stack-scatter background events, the cuts with the most powerful rejection were the range-stack quality cuts and the photon veto. The  $K_{\pi 2}$  range-stack-scatter normalization branch was a modified version of the  $K_{\pi 2}$  target-scatter normalization branch, with the range-stack quality cuts inverted instead of being applied before the inversion the PV cut as was done in the  $K_{\pi 2}$  target-scatter normalization branch. This sample of 281 events was heavily contaminated with target-scatter

events due to the inefficiency of the range-stack-scatter cuts. By exploiting the events remaining at the end of the  $K_{\pi 2}$  target-scatter and  $K_{\pi 2}$  range-stack-scatter normalization branches and the measured performance of the range-stack quality cuts relative to  $K_{\pi 2}$  range-stack-scatter and signal events, it was possible to estimate the number of  $K_{\pi 2}$  range-stack-scatter events present in the original  $K_{\pi 2}$  target-scatter normalization branch, giving  $23.3 \pm 3.5^{+2.9}_{-3.0}$   $K_{\pi 2}$  range-stack-scatter events in region B.

The  $K_{\pi 2}$  range-stack-scatter rejection branch was created by applying all analysis cuts other than the PV cut and the signal phase space cuts in the KIN cuts. Instead the  $K_{\pi 2}$  phase space cuts were applied, creating a sample of  $K_{\pi 2}$  events that did not scatter in the target, giving 122 581 events for the region C + D. The PV cuts (CUT1) were then applied to the remaining  $K_{\pi 2}$ , leaving 106 events in region C.

The  $K_{\pi 2\gamma}$  background estimate was performed using a combination of  $K_{\pi 2}$  data and simulated  $K_{\pi 2(\gamma)}$  events. Given a measured number of  $K_{\pi 2\gamma}$  events in the Kp2-peak (FIXME - define Kp2-peak), the simulated events were used to predict the number of  $K_{\pi 2(\gamma)}$  events that would have shown up in the signal region, taking into account the additional photo veto rejection due to the radiative photon. This additional rejection was calculated by combining the distribution of the radiative photon from simulated events with the single photon detection efficiency as a function of angle and energy from  $K_{\pi 2}$  data [FIXME - add citation].

The inverted photon veto used to select events for the  $K_{\pi 2}$  target-scatter normalization branch would have enhanced the  $K_{\pi 2\gamma}$  contamination in this branch due to the presence of the radiative photon. Using  $K_{\pi 2}$  monitor triggers it was shown that the  $K_{\pi 2}$  target-scatter normalization branch consisted of as much as 30%  $K_{\pi 2\gamma}$  events. Based on this upper limit, it was determined that the contributions to the total background due to  $K_{\pi 2\gamma}$  events were being entirely double-counted between the  $K_{\pi 2\gamma}$  and  $K_{\pi 2}$  target-scatter background estimates. To correct for this double-counting the  $K_{\pi 2\gamma}$  was subtracted from the  $K_{\pi 2}$  target-scatter background.

## 2. $K_{e4}$ background

The  $K^+ \rightarrow \pi^+ \pi^- e^+ \nu$  ( $K_{e4}$ ) decay with a branching fraction of  $(4.09 \pm 0.10) \times 10^{-5}$  [9] and with the  $\pi^+$  maximum momentum at 203 MeV/c could be a serious background in the  $\pi\nu\bar{\nu}(2)$  region due to the lack of photon in the final state to veto and a large fraction of the decay  $\pi^+$  phase space falling in the kinematic signal region. The low energy  $\pi^-$  and the  $e^+$  might not leave the target and escaped detection by depositing their energy in kaon and pion fibers or insensitive materials. For a combined total kinetic energy ( $T_2$ ) of the  $\pi^-$  and the  $e^+$  below 80 MeV, the  $\pi^+$  momentum congregated at around 160 MeV/c (see Fig. 6)

The main characteristic of  $K_{e4}$  event was extra en-

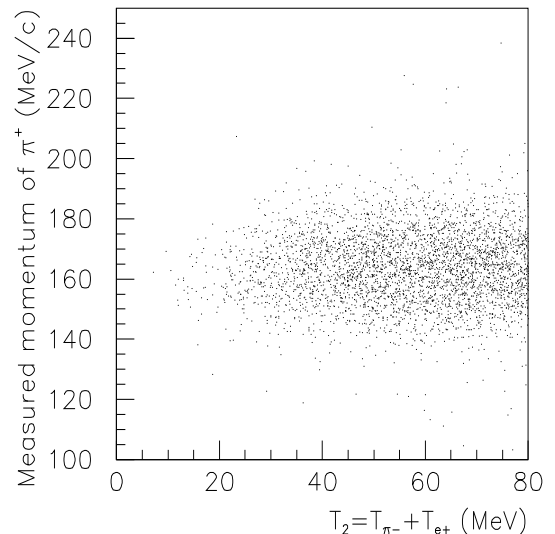


FIG. 6: Total kinetic energy ( $T_2$ ) of the  $\pi^-$  and the  $e^+$  versus the measured momentum of the  $\pi^+$  for Monte Carlo events that passed the trigger.

ergy deposit in the target from the  $\pi^-$  and the  $e^+$ . TGPV, OPSVETO and CCDPUL (JARGON? **FIXME**) cut were the most effective cuts to suppress this background. Due to the low statistic and contamination with other type of background it was very difficult to isolate a pure  $K_{e4}$  background sample to do bifurcation analysis. A  $K_{e4}$  rich sample was tagged by  $\text{TGPV} \cdot \text{OPSVETO}$  and used as normalization branch. These events were scanned by eye and the majority of them were likely to be  $K_{e4}$  candidates. The momentum distribution of the normalization branch without CCD pulse requirement was shown in Fig. 7 which was consistent with  $K_{e4}$  assumption like MC events in Fig. 6. MC study was used to determine the total rejection of the  $\text{TGPV} \cdot \text{OPSVETO}$ . To model  $\pi^-$  absorption in the target an empirical stopped  $\pi^-$  energy spectrum in plastic scintillator was got based on a measurement of stopped  $\pi^-$  in range stack where it had the same material as the target and a good  $\pi^-$  identification was available. The rejection of CCDPUL and  $\text{TGPV} \cdot \text{OPSVETO}$  were physically correlated with respect to the  $K_{e4}$  background because the additional energy of the  $\pi^-$  and  $e^+$  was blindly deposited in either kaon or pion fibers. This feature was also studied by MC where the CCD pulse information was from MC truth.

The  $K_{e4}$  background was measured to be  $0.176 \pm 0.072^{+0.233}_{-0.124}$  where the first error was statistical and the second was systematic. The relatively large systematic error was due to the lack of a reliable CCD pulse simulation which was not practical because it would involve the simulation of every CCD device and offline pulse recognition. The systematic error was estimated by varying CCDPUL cut threshold in MC in its full possible range.

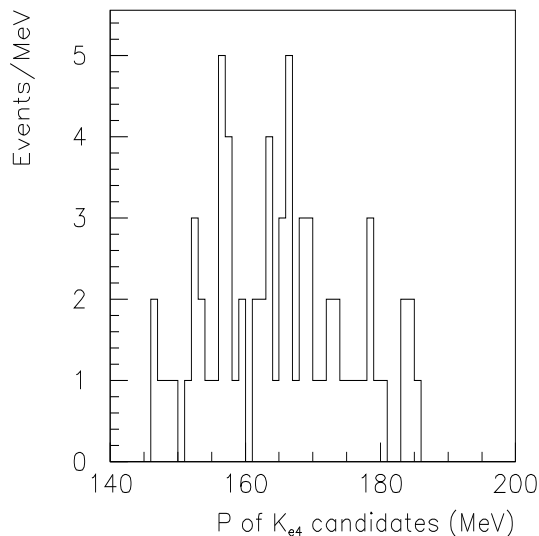


FIG. 7: Momentum distribution of  $K_{e4}$  normalization branch before CCD pulse cut.

### 3. Charge exchange background

The incident  $K^+$  might interact with the proton or neutron of the target nucleus. In the low energy range pion production from  $K^+$  and nucleon scattering was negligible. However the charge exchange process (CEX) interaction of  $K^+$  with a neutron could emit a  $K^0$  and a proton. The underlying interaction was expressed as  $K^+ + n \rightarrow K^0 + p$ . This was the only nuclear interaction which could contribute a new background since when  $K^+$  was closing to stop in target the energy was low enough that the recoil nucleus or proton was not detectable.

One background source that CEX brought in was the semi-leptonic decay of  $K_L^0$ ,  $K_L^0 \rightarrow \pi^+ e^- \nu_e$  and  $K_L^0 \rightarrow \pi^+ \mu^- \nu_\mu$  with branching ratios of 20% and 14%. The  $K^0$  could be either the shorter lifetime  $K_S^0$  (0.09ns) or the longer lifetime  $K_L^0$  state (51ns). An endothermic CEX process and a prompt  $K_S^0$  decay would not meet the delay coincidence requirement.

The other possible case was hyperon,  $\Sigma$  and  $\Lambda$ , production where a  $\pi^+$  was generated accompanied with the hyperon or a  $\pi^+$  was the decay product of hyperon because  $K^0$  might oscillate to a  $\bar{K}^0$  which contained a s quark and could interact with nucleon. The lifetime of  $K_L^0$  in the target would become shorter since there were another open channels for  $\bar{K}^0$ . Enumerate all the possible hyperon production processes there was always a  $\pi^-$  or  $\pi^0$  with momentum above 100 MeV/c coming along with  $\pi^+$ .

MC studies showed that there was often a gap between pion fiber and kaon fiber and the z information of the pion track was not consistent with vertex fiber, see the schematic diagram in Fig. 8. A CEX rich sample was tagged as normalization branch by selecting event which had a gap between pion and kaon fiber. No energy cuts

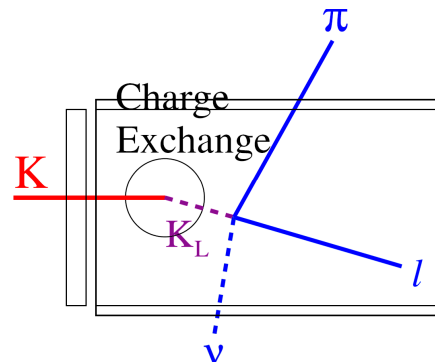


FIG. 8: Schematic diagram of the charge exchange interaction background

were applied in the target since the lepton from the semi-leptonic decay of  $K_L^0$  or the  $\pi^-$  and  $\pi^0$  from hyperon production might deposit extra energy in target. Delay coincidence was not required either which had large rejection to this background but could not be revealed by normalization branch limited by the low statistic. The probability of finding a gap in the CEX events and the rejection of energy cuts in the target and delay coincidence were studied by MC. For the simulation of CEX background  $K_S^0 \rightarrow \pi^+ \pi^-$  triggered and reconstructed events were used. Information concerning  $K_L^0$  production point and momentum vector were thus obtained from data. The shortened  $K_L^0$  lifetime was not taken into account. The background was measured to be  $0.013 \pm 0.013^{+0.010}_{-0.003}$  where the first error was statistical and the second for systematic. The systematic error outlined the rejection variance by changing target energy cuts in MC to all possible values which was the dominant error source.

### 4. Muon background

The  $\mu^+$  background consisted of the  $\mu^+$  band events consisting of  $K^+ \rightarrow \mu^+ \nu \gamma$  and  $K^+ \rightarrow \mu^+ \pi^0 + \nu$  which naturally occur in the  $\pi \nu \bar{\nu}(2)$  kinematic region as indicated in Figure ?? **FIXME: add figure?.** The  $K_{\mu 2}$  peak events and  $K_{\mu 2}$  range-tail events, as seen in Figure ?? are not backgrounds for the  $\pi \nu \bar{\nu}(2)$  analysis, unlike the  $\pi \nu \bar{\nu}(1)$  analysis, because of the large kinematic separation of the events to the  $\pi \nu \bar{\nu}(2)$  kinematic signal region.

The two bifurcation cuts were the TD cuts (CUT1) and the  $\pi/\mu$  range-momentum separation (CUT2) **FIXME: need to verify name previously used.** The CUT1 bifurcation was performed with the loose and tight versions of TD cuts to obtain a value of rejection for both. To avoid invaliding the blinded signal region, the loose TD cut was inverted for both the loose and tight iterations of the normalization branch which yielded zero events, so the value was assigned to be  $B = 1 \pm 1$ .

The  $\mu^+$  background sample was selected by applying the beam cuts to remove beam backgrounds, a loose version of PV cuts with 95% acceptance. To increase statistics within the background sample the nominal PV cuts which removed  $K_{\pi 2}$  events and kinematic cuts which removed  $K_{\mu 2}$  peak events were not applied which yielded a loose (tight) sample with  $C + D = 20488$  (18411) events. After the application of the loose (tight) TD cuts, the number of events remaining were  $C = 154$  (45) for a final measured loose (tight) TD cut rejection of  $133.04 \pm 10.68$  ( $409.13 \pm 60.92$ ). Thus, the  $\mu^+$  background for the loose signal region was measured to be  $0.0114 \pm 0.0114$ .

### 5. Beam background

*Single Beam Background* The bifurcation cuts for single beam background was delayed coincidence (CUT1) and B4 energy loss of less than 1.0 MeV, which selects beam pions, (CUT2) **FIXME: not sure of name used in PRD**. The sample was selected by applying PV cuts (not including the target category), kinematic cuts, TD cuts, beam cuts except delayed coincidence, and CUT2. The loose (tight) rejection sample contained  $C + D = 12850$  (7780) events such that after the application of the loose (tight) delayed coincidence only  $C = 2$  (1) events remained. Thus, the rejection of the loose (tight) delayed coincidence cut was measured to be  $6425.0 \pm 4542.8$  ( $7780.0 \pm 7779.5$ ). The normalization sample which inverted the loose delayed coincidence for both the loose and tight samples yielded zero events, so that  $B$  was assigned to be equal to  $1 \pm 1$ . The measured single beam background was  $0.00023 \pm 0.00023$ .

*Double Beam Background*

### 6. Background contamination evaluation

Data-driven studies were used to estimate the degree of contamination in the  $K_{\pi 2}$  target-scatter normalization and rejection branches due to muon-based and double-beam events. Bifurcation studies performed in each of these branches limited the contamination to on the order of 1% due to each of the muon-based, double-beam  $K^+ - K^+$  and double-beam  $K^+ - \pi^+$  backgrounds. It was also shown that the  $K_{e4}$  normalization branch was a subset of the  $K_{\pi 2}$  target-scatter normalization branch, limiting  $K_{e4}$  contamination in the  $K_{\pi 2}$  target-scatter normalization branch to  $< 1\%$ .

### 7. Background consistency checks

The reliability of the bifurcation method used to estimate the backgrounds relied on the two bifurcation cuts being uncorrelated. Three distinct data regions just outside the signal region were created by loosening the photon veto cut (regions PV<sub>1</sub> and PV<sub>2</sub> in Figure xxx - FIXME -

TABLE II: Acceptance factors of the  $K^+ \rightarrow \pi^+ \nu \bar{\nu}$  selection criteria measured with  $K_{\mu 2}$  monitor trigger data. Only statistical uncertainties are shown. The product is  $A_{K_{\mu 2}}$ .

Cut	Acceptance factor
Range stack track reconstruction	$0.99993 \pm 0.00001$
UTC-range stack track matching	$0.99943 \pm 0.00002$
Beam and target pattern	$0.15081 \pm 0.00018$
Photon veto	$0.48122 \pm 0.00200$
$A_{K_{\mu 2}}$	$0.07253 \pm 0.00031$

this will be a custom OTB figure with the PV and CCD cuts as axes and the 3 OTB regions used clearly defined) or target pulse-shape cuts (region CCD<sub>1</sub> in Figure xxx-FIXME no fig yet). For uncorrelated cuts the number of observed events should be consistent with the number of events expected in that region using the bifurcation method. The region CCD<sub>1</sub> was the region immediately adjacent to the signal region defined by loosening the pion energy thresholds from 1.25 MeV to 2.5 MeV for pion energy under target fiber classified as both a  $K^+$  and  $\pi^+$  fiber, pion energy from target CCD fitting, bad results from CCD fitting, and bad timing results from CCD fitting cuts. The region PV<sub>1</sub> was the region immediately adjacent to the signal region defined by loosening the nominal photon veto from an acceptance of 62.0% to an acceptance of 89.6%. The region PV<sub>2</sub> was the region adjacent to PV<sub>1</sub>, bounded by PV<sub>1</sub> and the pnn1-level photon veto which had an acceptance of 92.5%.

Table xxx (FIXME - reproduce PRL table) shows the number of expected and observed events as well as the probability of observation. FIXME - restate David's PRL description of the probabilities.

### 8. Single-cut failure study

#### D. Acceptance and sensitivity

We assessed the acceptance of the selection criteria by dividing the criteria into components that could be measured separately using monitor triggers or simulated data. Simulated data were used to estimate the acceptance of trigger and decay phase space as well as to assess the impact of nuclear interactions.

*Acceptance factors from  $K_{\mu 2}$  events*

$K_{\mu 2}$  monitor triggers were used to assess the components of the acceptance regarding the kaon beam, the charged track and the event topology. The acceptance factors are listed in Table II and described below.

To measure the acceptance of the range stack track reconstruction, a sample of  $K_{\mu 2}$  monitor triggers was selected by requiring a good track in the target and UTC, an energy deposit in the B4 hodoscope consistent with an entering kaon and a delayed-coincidence of  $> 5$  ns based on the  $\bar{C}_K$  and the IC. The acceptance of the range stack tracking cuts on the surviving  $K_{\mu 2}$  events is given in second row of Table II.

TABLE III: Acceptance factors measured with  $K_{\pi 2}$  monitor trigger data. Uncertainties are statistical only. The product of all factors is  $A_{K_{\pi 2}}$ .

Cut	Acceptance factor
UTC reconstruction	$0.94345 \pm 0.00019$
OPSVETO	$0.97417 \pm 0.00063$
$\pi^+$ identification in target	$0.71851 \pm 0.00181$
$A_{K_{\pi 2}}$	$0.6604 \pm 0.0018$

The acceptance of consistency of the range stack and UTC track was assessed using a  $K_{\mu 2}$  sample with a good track in the range stack, a delayed-coincidence of  $> 5$  ns based on the  $\tilde{C}_K$  and the IC, and a single entering kaon selected based on the B4 energy deposit and the beam Čerenkov and wire chambers. The UTC-range stack track matching acceptance factor is given in the third row of Table II.

The acceptance factor associated with the beam and target pattern recognition was evaluated on a sample of  $K_{\mu 2}$  events that were required to have a single entering kaon and a good track in the UTC and range stack with  $|\cos\theta| < 0.5$ . In addition the momentum of the reconstructed track was required to be within two standard deviations of the expectation for  $K_{\mu 2}$  decays. There were over forty individual cuts associated with the beam and target pattern recognition as described in Section III B 1. The majority of the individual cuts had acceptance greater than 90% except for the delayed-coincidence (75.5%) and the CCDPUL (45.1%) requirements. The fourth row of Table II contains the overall acceptance factor of the beam and target cuts.

To measure the acceptance of the photon veto, an additional criterion was applied to the  $K_{\mu 2}$  events used for the beam and target acceptance. As muons from  $K_{\mu 2}$  decay can penetrate into the barrel veto, the reconstructed track was required to stop before the outermost layer of the range stack. The acceptance factor given in Table II evaluated in this manner yielded the overall acceptance of both the online and offline photon veto cuts as the  $K_{\mu 2}$  monitor trigger did not include the photon veto.

#### Acceptance factors from $K_{\pi 2}$ events

The  $K_{\pi 2}$  monitor data was used to assess the acceptance factors associated with charged track reconstruction in the UTC and pion identification in the target. The acceptance of the veto of an additional track in the target (OPSVETO, Section III B 1) was measured with  $K_{\pi 2}$  monitors. The factors are listed in Table III and described below.

To measure the acceptance of the UTC reconstruction, events from the  $K_{\pi 2}$  monitor trigger were required to have a well-reconstructed track in the range stack and agreement between the online and offline determination of the range stack stopping counter. The factor is given in the second row of Table III.

For the measurement of the acceptance of the OPSVETO cut, in addition to the requirements described above, the charged track was required to be well-

reconstructed in the UTC and range stack, identified as a pion based on the measured range and momentum as well as the  $\pi \rightarrow \mu \rightarrow e$  signature in the stopping counter and kinematically consistent with the pion from a  $K_{\pi 2}$  decay. Cuts were also applied to ensure a single kaon entered the target. The acceptance factor for the OPSVETO is presented in the third row of Table III.

In addition to the requirements described above, the OPSVETO and target photon veto cuts were applied to the  $K_{\pi 2}$  monitor events to assess the cumulative acceptance of the ten pion identification cuts in the target. These ten cuts were designed to reject tracks that contained an indication of a kink or discontinuity in the pattern of target fibers or target fibers with an unexpected energy deposit (Section III B 1). The acceptance factor for these cuts is listed in the fourth row of Table III. Two individual cuts with less than 90% acceptance were the requirement that no individual pion fiber had more than 3 MeV (89.6%) and the requirement on that the pattern of energy deposits in the target fibers was consistent with an unknicked pion trajectory (87.4%).

#### Acceptance factors from $\pi_{\text{scat}}$ events

Beam pions that scatter in the target have a spectrum of range, energy and momentum similar to that of pions from  $K^+ \rightarrow \pi^+ \nu \bar{\nu}$  and were used to determine the acceptance factors associated with the reconstruction and identification of pions in the range stack. Table IV lists the acceptance factors measured using  $\pi_{\text{scat}}$  monitors.

Candidate events were rejected if the pion stopped in a counter with a non-operational TD. The acceptance factor associated with this requirement was measured on a sample of  $\pi_{\text{scat}}$  monitor data selected by requiring a good outgoing track in the range stack, drift chamber, and target, a delayed-coincidence of less than 5 ns, a single pion entering the target and range, energy and momentum in the signal region. The acceptance factor is given in the second row of Table IV.

In addition to the requirements listed above,  $\pi_{\text{scat}}$  monitor data was also required to have a good  $\pi \rightarrow \mu \rightarrow e$  signature and the pion was required to stop in range stack counter with an operational TD in order to measure the acceptance factor associated with the range stack kinematics and tracking. Assignment of target fibers to the incoming and outgoing pion in  $\pi_{\text{scat}}$  was not as robust as the assignments made for kaon decays at rest. Misassignment of target fibers yielded a larger uncertainty in the momentum, range and energy calculated for the outgoing pion in  $\pi_{\text{scat}}$  events. The effect of increasing or decreasing the signal phase space by  $\pm 1$  standard was used to estimate the systematic uncertainty in this acceptance factor that is shown in third row of Table IV.

The requirements used to assess the acceptance factor associated with a non-operational TD in the stopping counter were supplemented by requiring a good track in the drift chamber and range and momentum consistent with a pion in order to measure the acceptance factor associated with the  $\pi \rightarrow \mu \rightarrow e$  signature. The cut on the measured  $dE/dx$  in range stack counters and the cuts

TABLE IV: Acceptance factors measured with  $\pi_{\text{scat}}$  monitor triggers. Operational is abbreviated as “Oper.” The first and second uncertainties are statistical and systematic, respectively. The assessment of systematic uncertainties is described in the text.  $A_{\pi_{\text{scat}}}$  is the product of the three acceptance factors.

Cut	Acceptance factor
Oper. TD in stopping counter	$0.99843 \pm 0.00010$
Range stack kinematics	$0.82594 \pm 0.00126 \pm 0.01200$
$\pi \rightarrow \mu \rightarrow e$ signature	$0.4805 \pm 0.0015 \pm 0.0160$
$A_{\pi_{\text{scat}}}$	$0.3980 \pm 0.0014 \pm 0.0140$

TABLE V: Acceptance factors determined from simulated  $K^+ \rightarrow \pi^+ \nu \bar{\nu}$  decays.  $A_{MC}$  is the product of the three acceptance factors.

Component	Acceptance factor
Trigger	$0.3225 \pm 0.0015$
Phase space	$0.3650 \pm 0.0027$
$\pi^+$ -nuclear interactions	$0.8284 \pm 0.0104$
$A_{MC}$	$0.0975 \pm 0.0009$

on the consistency of the range stack and drift chamber track had some correlation with the suite of cuts used to define the  $\pi \rightarrow \mu \rightarrow e$  signature. The acceptance factor of the  $\pi \rightarrow \mu \rightarrow e$  signature was assessed both with and without these cuts applied to estimate the systematic uncertainty due to these correlations. In addition a correction of 1.0% for pion decay-in-flight and pion absorption in the stopping counter, estimated from Monte Carlo, was applied to the acceptance factor given in the fourth row of Table IV.

#### Acceptance factors from simulated events

Simulated  $K^+ \rightarrow \pi^+ \nu \bar{\nu}$  events were used to evaluate the trigger acceptance and the acceptance associated with phase space and  $\pi^+$ -nuclear interactions. The acceptance of the  $L1.1$  and  $L1.2$  ( $DC'$ ) components of the trigger as described in Section II were evaluated with  $K_{\pi 2}$  ( $K_{\mu 2}$ ) monitors as described previously in this Section. The acceptance of the remaining trigger components is given in the second row of Table V. The phase space acceptance of the events surviving the trigger simulation is shown in the third row of the Table. The phase space acceptance includes the loss due to  $\pi^+$  absorption and decay in flight. Neither the trigger or phase space acceptance include the effect of nuclear interactions. As indicated in Section III A, the combined trigger and phase space acceptance factor of 11.8% was larger than the corresponding factor of 6.5% for the  $\pi \nu \bar{\nu}(1)$  region [1]. The acceptance factor associated with  $\pi^+$ -nuclear interactions was evaluated separately and is given in the fourth row of Table V. For the  $\pi \nu \bar{\nu}(1)$  region, the acceptance factor due to nuclear interactions was 49.5% [1].

#### Correction to the $T \cdot 2$ efficiency

The  $T \cdot 2$  component of the trigger (Section II) required a coincidence between range stack counters in the same sector in the two innermost layers and in the IC. The simulation did not include the acceptance loss due to gaps

between the neighboring T counters or due to insufficient scintillation light in the thin T counters. These acceptance losses were measured by using  $K_{\mu 2}$  and  $K_{\pi 2}$  decays in KB monitor events. The energy loss in the T counter by the charged track differs for  $K_{\mu 2}$  and  $K_{\pi 2}$  events and simulated events were used to obtain the average energy loss for each decay. The measured acceptance factors for  $K_{\mu 2}$  and  $K_{\pi 2}$  were then extrapolated to estimate

$$A_{T \cdot 2} = 0.9505 \pm 0.0012 \pm 0.0143 \quad (3)$$

where a  $\pm 1.5\%$  systematic uncertainty was assigned to account for the extrapolation of the drift chamber track to the T counter.

#### Normalization to the $K_{\mu 2}$ branching ratio

We assessed the fraction ( $f_s$ ) of  $K^+$  that stopped in the target by normalization to the  $K_{\mu 2}$  branching ratio [9] as described in [1]

$$f_s = 0.7740 \pm 0.0011 \quad (4)$$

#### Confirmation of the $K_{\pi 2}$ branching ratio

We measured the  $K_{\pi 2}$  branching fraction using the  $K_{\pi 2}$  monitor trigger data in order to confirm the validity of the acceptance factors and corrections calculated with data and Monte Carlo. Our measurement followed the same analysis procedure as described in [1] but utilized the selection criteria developed for the pnn2 analysis. From this analysis we obtained

$$\mathcal{B}(K^+ \rightarrow \pi^+ \pi^0) = 0.221 \pm 0.002 \quad (5)$$

where the uncertainty is statistical. This is in reasonable agreement with the world average value [9] of  $0.209 \pm 0.001$  for the branching fraction.

#### Overall acceptance and sensitivity

The total acceptance was evaluated as the product of  $A_{K_{\pi 2}}$ ,  $A_{K_{\mu 2}}$ ,  $A_{\pi_{\text{scat}}}$ ,  $A_{MC}$ ,  $f_s$  and  $A_{T \cdot 2}$  or  $(1.37 \pm 0.14) \times 10^{-3}$  where we assigned a 10% uncertainty on the total acceptance to accommodate the discrepancy in  $\mathcal{B}(K^+ \rightarrow \pi^+ \pi^0)$  and the additional systematic and statistical uncertainties in the acceptance evaluated in this Section. Based on the total exposure of  $1.7 \times 10^{12}$  stopped kaons for this analysis, the single event sensitivity (SES) of the  $\pi \nu \bar{\nu}(2)$  analysis was  $\text{SES} = (4.28 \pm 0.43) \times 10^{-10}$  which can be compared with the SES of the E949  $\pi \nu \bar{\nu}(1)$  analysis of  $(2.55 \pm 0.20) \times 10^{-10}$  [1] and the combined SES of the previous  $\pi \nu \bar{\nu}(2)$  analyses of  $(6.87 \pm 0.04) \times 10^{-10}$  with the E787 apparatus [7, 8].

## IV. RESULTS

In this Section, we describe the likelihood method used to evaluate the  $K^+ \rightarrow \pi^+ \nu \bar{\nu}$  branching fraction and the results of examining the signal region. We also describe the evaluation of our observations within alternative models of  $K^+ \rightarrow \pi^+$  nothing.

TABLE VI: The estimated signal-to-background ( $s/b$ ), background ( $b$ ) and observed number of candidates for the nine cells. The cuts defining each cell are also given. The  $s/b$  is calculated assuming  $\mathcal{B}(K^+ \rightarrow \pi^+ \nu \bar{\nu}) = 1.73 \times 10^{-10}$ . The uncertainties on  $b$  and  $s/b$  are omitted from the table. The definition column indicates the whether the tight version of the kinematics (KIN), photon veto (PV), delayed coincidence (DC) or  $\pi \rightarrow \mu \rightarrow e$  (TD) cut or the inverted cut (*i.e.*,  $\overline{\text{KIN}}$ ) was applied to define the cell. The cells containing signal candidate events A, B and C are indicated.

Cell definition	$b$	Candidates	$s/b$
KIN · TD · DC · PV	0.152	0	0.84
KIN · $\overline{\text{TD}}$ · DC · PV	0.038	0	0.78
KIN · TD · $\overline{\text{DC}}$ · PV	0.019	0	0.66
KIN · $\overline{\text{TD}}$ · $\overline{\text{DC}}$ · PV	0.005	0	0.57
KIN · TD · DC · $\overline{\text{PV}}$	0.243	1 B	0.47
KIN · $\overline{\text{TD}}$ · DC · $\overline{\text{PV}}$	0.059	0	0.45
KIN · TD · $\overline{\text{DC}}$ · $\overline{\text{PV}}$	0.027	1 C	0.42
KIN · $\overline{\text{TD}}$ · $\overline{\text{DC}}$ · $\overline{\text{PV}}$	0.007	0	0.35
$\overline{\text{KIN}}$	0.379	1 A	0.20

### A. Likelihood method

We determined  $\mathcal{B}(K^+ \rightarrow \pi^+ \nu \bar{\nu})$  using a likelihood method that took into account the distributions of the predicted background and acceptance within the signal region. The signal region was divided into nine cells with differing acceptance-to-background ratios as described below. The likelihood ratio  $X$  was defined as

$$X \equiv \prod_{i=1}^n \frac{e^{-(s_i+b_i)} (s_i+b_i)^{d_i}}{d_i!} \bigg/ \frac{e^{-b_i} b_i^{d_i}}{d_i!} \quad (6)$$

where  $s_i$  and  $b_i$  were the estimated signal and background in the  $i^{\text{th}}$  cell,  $d_i$  was the observed number of signal candidates in the  $i^{\text{th}}$  cell and  $n$  was the total number of cells [10]. The estimated signal in each cell was given by  $s_i \equiv \text{SES}_i \times \mathcal{B}(K^+ \rightarrow \pi^+ \nu \bar{\nu})$  where  $\text{SES}_i$  was the single event sensitivity of the  $i^{\text{th}}$  cell.

The division of signal region into nine cells was performed using combinations of the kinematics (KIN), photon veto (PV), delayed coincidence (DC) or  $\pi \rightarrow \mu \rightarrow e$  (TD) cuts. We defined a standard and a more restrictive or “tight” version of each cut. The signal region was defined by the application of the standard version of all cuts. The signal region was then subdivided into cells by the additional selective application of the tight version of each cut or the inverted cut as shown in Table VI.

The additional signal acceptance factor and rejection (Table VII) for each of the four tight cuts was determined using analogous techniques and samples as described in Section III D. Based on studies of data and simulated events, we assumed that the background components for which no rejection is given in the Table were reduced by the acceptance factor of the particular cut. For example, the acceptance of the cell defined by KIN ·  $\overline{\text{TD}}$  ·  $\overline{\text{DC}}$  · PV relative to the acceptance for the entire signal region was

TABLE VII: Additional acceptance factor ( $A$ ) or rejection ( $R$ ) for the tight version of the kinematics (KIN), photon veto (PV), delayed coincidence (DC) or  $\pi \rightarrow \mu \rightarrow e$  (TD) cuts for specific backgrounds.

	KIN	TD	DC	PV
$A$	0.812	0.812	0.911	0.522
$R$	1.63( $K_{\pi 2}$ ) 2.70( $K_{e 4}$ ) 1.20( $K_{\pi 2 \gamma}$ )	3.08 (Muon)	6.3 (CEX) 1.0 (Beam)	2.75 ( $K_{\pi 2(\gamma)}$ )

TABLE VIII: Range, energy and momentum of the  $\pi^+$  in the signal candidate events A, B and C as well as the measured  $K^+$ ,  $\pi^+$  and  $\mu^+$  lifetimes.

Candidate	A	B	C
Momentum (MeV/c)	161.5	188.4	191.3
Range (cm)	17.3	24.2	26.1
Kinetic energy (MeV)	76.1	95.6	97.9
$K^+$ lifetime (ns)	3.7	15.7	5.1
$\pi^+$ lifetime (ns)	22.4	16.7	10.2
$\mu^+$ lifetime (ns)	5959.4	2270.6	9507.8

$A_{\text{KIN}} \times (1 - A_{\text{TD}}) \times (1 - A_{\text{DC}}) \times A_{\text{PV}}$  with obvious notation and the  $K_{\pi 2}$ -target-scatter background component relative to the contribution to the entire signal region was reduced by the factor  $1/R_{\text{KIN}} \times (1 - A_{\text{TD}}) \times (1 - A_{\text{DC}}) \times 1/R_{\text{PV}}$ .

### B. Examination of the signal region

After completion of the background and acceptance analyses, all selection criteria were applied to the  $\pi \nu \bar{\nu}(1+2)$  trigger data and three signal candidate events were selected. Some measured properties of the three events are listed in Table VIII and the cells containing candidates A, B and C are given in Table VI. The kinetic energy vs. range of the three events along with the events found in the previous  $\pi \nu \bar{\nu}(1)$  [1] and  $\pi \nu \bar{\nu}(2)$  [7, 8] analyses are shown in Figure 9. The candidates’s measured properties used in the selection criteria were consistent with the expected distributions for signal. There was no observed activity in the kaon fibers at the time of the  $\pi^+$  for any of the three candidates according to the CCD-PUL analysis. The  $\pi^+$  momentum of event A fails the KIN cut of 165 MeV/c. Events B and C fail the tight PV cut due to energy deposits of 2.4 and 2.1 MeV in the end cap above the 1.7 MeV threshold, respectively, and event C fails the tight DC cut of 6 ns on the kaon lifetime.

### C. The $K^+ \rightarrow \pi^+ \nu \bar{\nu}$ branching ratio

The central value of the  $K^+ \rightarrow \pi^+ \nu \bar{\nu}$  branching ratio was taken to be the value of  $\mathcal{B}(K^+ \rightarrow \pi^+ \nu \bar{\nu})$  that maximized  $X$  (Eqn 6) given the observed candidates. For the three events observed by this analysis, we determined  $\mathcal{B}(K^+ \rightarrow \pi^+ \nu \bar{\nu}) = (7.89_{-5.10}^{+9.26}) \times 10^{-10}$  where the quoted 68% confidence level interval was determined from the



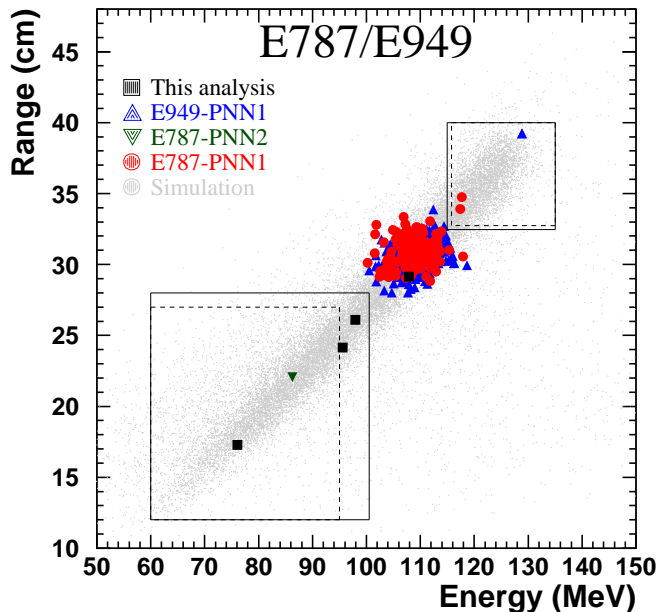


FIG. 9: Kinetic energy vs. range of all events passing all other cuts. The squares represent the events selected by this analysis. The circles and upward-pointing triangles represent the events selected by the E787 and E949 pnn1 analyses, respectively. The downward-pointing triangles represent the events selected by the E787 pnn2 analyses. The solid (dashed) lines represent the limits of the pnn1 and pnn2 signal regions for the E949 (E787) analyses. Despite the smaller signal region in  $E_\pi$  vs.  $R_\pi$ , the pnn1 analyses were 4.2 times more sensitive than the pnn2 analyses. The points near  $E_\pi = 108$  MeV were  $K_{\pi 2}$  decays that survived the photon veto cuts and were predominantly from the pnn1 analyses due to the higher sensitivity and the less stringent photon veto cuts. The light gray points are simulated  $K^+ \rightarrow \pi^+ \nu \bar{\nu}$  events that would be accepted by our trigger.

behavior of  $X$  as described in [10] and took into account both the statistical and systematic uncertainties. The systematic uncertainties included the 10% uncertainty in the acceptance as well as the uncertainties in the estimation of the background components. The inclusion of systematic uncertainties had a negligible effect on the confidence level interval due to the poor statistical precision inherent in a three event sample. The probability that these three events were due to background only, given the estimated background in each cell (Table VI), was 0.037.

When the results of the previous  $\pi \nu \bar{\nu}(1)$  and  $\pi \nu \bar{\nu}(2)$  analyses [1, 7, 8] were combined with the results of this analysis, we found  $\mathcal{B}(K^+ \rightarrow \pi^+ \nu \bar{\nu}) = (1.73^{+1.15}_{-1.05}) \times 10^{-10}$ . Systematic uncertainties were treated as described above when performing the combination, except that we assumed a correlated 10% un-

TABLE IX: The  $K^+ \rightarrow \pi^+ \nu \bar{\nu}$  branching ratio measurements in units of  $10^{-10}$ . The prediction was taken from [11] and scaled to the two pion momentum regions using the standard model spectral shape for  $K^+ \rightarrow \pi^+ \nu \bar{\nu}$ .

Momentum range (MeV/c)	Prediction	Measurement
[130, 205]	$0.49 \pm 0.04$	$2.91^{+4.02}_{-1.79}$
[205, 227]	$0.28 \pm 0.02$	$0.49^{+0.45}_{-0.29}$
All	$0.85 \pm 0.07$	$1.73^{+1.15}_{-1.05}$

certainty for the acceptance assessed by each analysis. The probability that all seven events were due to background (background and standard model signal) was 0.001 (0.073). We used a similar procedure to determine the partial branching fractions of  $(2.91^{+4.02}_{-1.79}) \times 10^{-10}$  and  $(0.49^{+0.45}_{-0.29}) \times 10^{-10}$  for the pion momentum ranges of (140, 205) and (205, 227) MeV/c, respectively, which can be compared with the standard model expectations of  $0.48 \times 10^{-10}$  and  $0.28 \times 10^{-10}$ .

## V. CONCLUSION

[1] S. Adler et al., Phys. Rev. **D77**, 052003 (2008), arXiv:0709.1000.  
[2] D. A. Bryman et al., Nucl. Instrum. Meth. **A396**, 394 (1997).  
[3] M. Atiya, M. Ito, J. Haggerty, C. Ng, and F. W. Sippach, Nucl. Instrum. Meth. **A279**, 180 (1989).  
[4] E. W. Blackmore et al., Nucl. Instrum. Meth. **A404**, 295 (1998).  
[5] I. H. Chiang et al., IEEE Trans. Nucl. Sci. **42**, 394 (1995).  
[6] T. K. Komatsubara et al., Nucl. Instrum. Meth. **A404**, 315 (1998).

[7] S. Adler et al., Phys. Lett. **B537**, 211 (2002), hep-ex/0201037.  
[8] S. Adler et al., Phys. Rev. **D70**, 037102 (2004), hep-ex/0403034.  
[9] W. M. Yao et al., J. Phys. **G33**, 1 (2006).  
[10] T. Junk, Nucl. Instrum. Meth. **A434**, 435 (1999), hep-ex/9902006.  
[11] J. Brod and M. Gorbahn, Phys. Rev. **D78**, 034006 (2008), arXiv:0805.4119. The uncertainty in the prediction is dominated by the uncertainty in the elements of the CKM matrix.